Signal Processing 92 (2012) 2082–2096

Contents lists available at SciVerse ScienceDirect

Signal Processing

journal homepage: www.elsevier.com/locate/sigpro

A super-resolution reconstruction algorithm for hyperspectral images

Hongyan Zhang [a], Liangpei Zhang [a,*], Huanfeng Shen [b]

[a] The State Key Laboratory of Information Engineering in Surveying, Mapping and Remote Sensing, Wuhan University, Wuhan, Hubei, China
[b] School of Resource and Environmental Science, Wuhan University, Wuhan, Hubei, China

ARTICLE INFO

Article history:
Received 1 August 2011
Received in revised form
24 November 2011
Accepted 21 January 2012
Available online 6 February 2012

Keywords:
Hyperspectral image
Super-resolution
Motion estimation
PCA

ABSTRACT

The spatial resolution of a hyperspectral image is often coarse because of the limitations of the imaging hardware. Super-resolution reconstruction (SRR) is a promising signal post-processing technique for hyperspectral image resolution enhancement. This paper proposes a maximum *a posteriori* (MAP) based multi-frame super-resolution algorithm for hyperspectral images. Principal component analysis (PCA) is utilized in both parts of the proposed algorithm: motion estimation and image reconstruction. A simultaneous motion estimation method with the first few principal components, which contain most of the information of a hyperspectral image, is proposed to reduce computational load and improve motion field accuracy. In the image reconstruction part, different image resolution enhancement techniques are applied to different groups of components, to reduce computational load and simultaneously remove noise. The proposed algorithm is tested on both synthetic images and real image sequences. The experimental results and comparative analyses verify the effectiveness of this algorithm.

1. Introduction

Hyperspectral sensors acquire images in many contiguous and very narrow spectral bands, which enable hyperspectral images to exploit fine spectral differences between various materials of interest. Therefore, hyperspectral images can support improved target detection and classification capabilities, relative to panchromatic and multispectral images [1]. Nowadays, hyperspectral images (HSI) are widely used in a variety of fields, including agriculture, ecology, geology, medicine, meteorology, and so on. However, a disadvantage of the hyperspectral image is that the spatial resolution is often coarser than that of panchromatic and multispectral images. This is an engineering tradeoff between spectral and spatial resolution, in order to maintain the high sensitivity in the spectral domain when designing the imaging hardware device. Therefore, it is necessary to develop signal post-processing techniques, in order to improve the spatial resolution of hyperspectral images.

Image super-resolution reconstruction (SRR) refers to a signal processing technique which produces a high-resolution (HR) image from a sequence of observed low-resolution (LR) images that are noisy, blurred and downsampled [2,3]. The SRR technique was first proposed by Tsai and Huang [4] in the frequency domain. They presented a formulation for the reconstruction of a HR image from a set of undersampled, aliased and noise-free LR images. Their method was then extended by Kim et al. [5] to consider observation noise, as well as the effects of spatial blurring. More recently, discrete cosine transform (DCT) based [6] and wavelet transform-based [7,8] SRR methods have also been proposed. Generally speaking, the frequency domain approaches have the strength of theoretical simplicity and high computational efficiency.

* Corresponding author. Tel.: +86 27 68778452; fax: +86 27 68778229.
E-mail addresses: zlp62@lmars.whu.edu.cn, zlp62@public.wh.hb.cn (L. Zhang).

0165-1684/$ - see front matter © 2012 Elsevier B.V. All rights reserved.
doi:10.1016/j.sigpro.2012.01.020

However, these methods are not able to accommodate spatial domain *a priori* knowledge, non-global translational motion models, or spatially varying degradation [2]. Consequently, many kinds of spatial domain approaches have been developed to overcome the weaknesses of the frequency domain approaches. Typical spatial domain reconstruction methods include: non-uniform interpolation [9], iterative back projection (IBP) [10], projection onto convex sets (POCS) [11–13], Bayesian/maximum *a posteriori* (MAP) [14–16], hybrid MAP/POCS [17], and adaptive filtering [18]. Currently, image SRR has a variety of applications, including remote sensing [19], video surveillance [20], medical diagnostics and military information gathering.

It is noted that most super-resolution methods, to date, have been designed for monochromatic or color images. In recent years, because of the potential of super-resolution reconstruction in the spatial resolution enhancement of images, scholars have begun to employ super-resolution reconstruction techniques to improve the spatial resolution of hyperspectral images. In [21], Akgun et al. proposed a complicated hyperspectral image acquisition model, with which a POCS-based super-resolution method was proposed to enhance the resolution of hyperspectral images. Buttingsrud and Alsberg proposed a maximum entropy-based hyperspectral image super-resolution reconstruction method in [22]. Mianji et al. studied the important problems and challenges in hyperspectral image super-resolution reconstruction [23]. However, most of these methods just used synthetic images, assuming known motion parameters in their experiments. As an alternative, many researchers have tackled the image fusion problem of improving the spatial resolution of a hyperspectral image, through using an auxiliary HR image. A typical example is the use of a panchromatic (PAN) image for sharpening hyperspectral images [1,24]. However, this type of method often destroys the spectral information, which is extremely important for the applications of hyperspectral images.

The most direct solution, for hyperspectral image super-resolution, is to apply super-resolution technology to every separate spectral band individually, but this has the following two problems. The first problem is the huge computational load arising from the high dimensionality of the hyperspectral images [21], which exists in both parts of the SRR procedure: motion estimation and image super-resolution reconstruction. Furthermore, high correlation exists across the spectral bands, so considering these bands separately will not fully exploit the correlation across them and results in spectral artifacts in the super-resolved hyperspectral images. In this paper, principal component analysis (PCA) is used to reduce the dimensionality of the hyperspectral image. It is well known that the first few principal components contain most of the information of the hyperspectral image, so we transform the super-resolution reconstruction of the hyperspectral image to that of its first few principal components in this paper, thereby greatly reducing the computational load of the proposed method.

This paper proposes a multi-frame image super-resolution reconstruction algorithm for hyperspectral images. The contributions of the paper are threefold. Firstly, we present a simultaneous motion estimation method, utilizing multiple components of the hyperspectral image to improve the accuracy of the motion parameters. The reason for this is that all the bands of the hyperspectral image convey the same motion information, which provides more information than a single band. Secondly, we introduce a MAP-based hyperspectral image super-resolution reconstruction algorithm, in which PCA is employed to reduce computational load and simultaneously remove noise. Experimental results show that our method not only improves the spatial resolution of the image effectively, but also preserves spectral information well. Thirdly, with the proposed motion estimation method, we conduct our experiments on real hyperspectral images. The experimental results validate the effectiveness of the proposed method.

The remainder of the paper is organized as follows. In Section 2, the hyperspectral image SRR observation model is described. The motion estimation method for hyperspectral images is introduced in Section 3. In Section 4, the MAP estimation-based hyperspectral image SRR algorithm is explained. Experimental results are provided in Section 5, and Section 6 concludes the paper.

2. Observation model

An image observation model is employed to relate the desired referenced HR image to the observed LR images. First, we study the image observation model in the single band (monochrome) case. Generally, the imaging process involves warping, followed by blurring and downsampling to generate LR images from the HR image. Let the underlying HR image be denoted in the vector form by $\mathbf{z}=[z_1,z_2,\ldots,z_{L_1N_1\times L_2N_2}]^T$, where $L_1N_1\times L_2N_2$ is the HR image size. Letting L_1 and L_2 denote the downsampling factors, in horizontal and vertical directions, respectively, each observed LR image has the size $N_1\times N_2$. Thus, the LR image can be represented as $\mathbf{g}_k=[g_{k,1},g_{k,2},\ldots,g_{k,N_1\times N_2}]^T$, where $k=1,2,\ldots,P$, with P being the number of LR images. Assuming that each observed image is contaminated by additive noise, the observation model can be represented as [4,25]

$$\mathbf{g}_k=\mathbf{D}\mathbf{B}_k\mathbf{M}_k\mathbf{z}+\mathbf{n}_k \tag{1}$$

where $\mathbf{M}_k$ is the warp matrix with the size of $L_1N_1L_2N_2\times L_1N_1L_2N_2$, $\mathbf{B}_k$ represents the camera blur matrix, also of size $L_1N_1L_2N_2\times L_1N_1L_2N_2$, $\mathbf{D}$ is a $N_1N_2\times L_1N_1L_2N_2$ downsampling matrix, and $\mathbf{n}_k$ represents the $N_1N_2\times 1$ noise vector. Extending this monochrome image observation model to the hyperspectral case, we can obtain the following model:

$$\mathbf{g}_{k,r}=\mathbf{D}\mathbf{B}_{k,r}\mathbf{M}_{k,r}\mathbf{z}_r+\mathbf{n}_{k,r} \tag{2}$$

where $r=1,2,\ldots,R$, with R being the number of spectral bands. As all the bands of the hyperspectral image convey the same motion information, the matrix $\mathbf{M}_{k,r}$ is substituted by matrix $\mathbf{M}_k$. Assuming that the blurring function remains the same for all the bands of the low-resolution hyperspectral observations, the matrix $\mathbf{B}_{k,r}$ will be substituted by matrix $\mathbf{B}$.

In this paper, a PCA transform is used to reduce the computational load of the hyperspectral image SRR process. PCA is a widely used dimensionality reduction technique in data analysis [26]. It computes the low-dimensional representation of a high-dimensional data set, which faithfully preserves the covariance structure. One needs to solve the eigenvalues and eigenvectors of the covariance matrix. The outputs of PCA are simply the coordinates of the input patterns in this subspace, using the directions specified by these eigenvectors as the principal axes [27].

Corresponding to the observation model relating the observed low-resolution hyperspectral image and the desired high-resolution hyperspectral image, we can set up the following observation model for the PCA components of hyperspectral images:

$$\mathbf{g}'_{k,r} = \mathbf{DBM}_k \mathbf{z}'_r + v_{k,r} \tag{3}$$

where $r=1,2,...,R$. Here $\mathbf{g}'_{k,r}$ and $\mathbf{z}'_r$ represent the rth principal component of the kth low-resolution hyperspectral observation and super-resolved hyperspectral image, respectively. $v_{k,r}$ represents the corresponding model noise of the rth principal component for the kth low-resolution observation.

It is believed that the first few principal components contain the most information, and the remaining principal components contain much less information. Therefore, the principal components of HSI are divided into three groups. The first R_1 components, containing most of the information of the original HSI, are referred to as primary components, and the last few components (from R_2 to R), with more noise and much less information, as noise components. The remaining components (from R_1 to R_2) are referred to as secondary components. As the primary components contain most of the information of the hyperspectral image, we only apply the computationally complicated SRR method to the primary components and employ other resolution enhancement methods, which are computationally efficient, to the other components. Therefore, the value of r in (3) ranges from 1 to R_1, forming the observation model for the primary components of the hyperspectral image.

3. Motion estimation method

Motion estimation plays an important role in SRR. The motion estimation method of a single-band (monochrome) image will be introduced first and then extended to the hyperspectral case. Generally speaking, the relationship between the rth band image of the kth and the lth low-resolution hyperspectral observations can be expressed as

$$\mathbf{g}_{k,r}(x,y) = f_{k,r}(l,\boldsymbol{\theta})(x,y) + \varepsilon_{k,l,r} \tag{4}$$

where (x,y) denotes the pixel location, $\mathbf{g}_{k,r}(x,y)$ represents a pixel in the rth band of frame k, $\boldsymbol{\theta}$ is the motion vector containing the corresponding motion parameters between frame k and frame l, $f_{k,r}(l,\boldsymbol{\theta})(x,y)$ represents the predicted pixel of $\mathbf{g}_{k,r}(x,y)$ from frame l with motion vector $\boldsymbol{\theta}$ and $\varepsilon_{k,l,r}$ is the model error. By assuming a six-parameter affine motion model, $f_{k,r}(l,\boldsymbol{\theta})(x,y)$ can be expressed as

$$f_{k,r}(l,\boldsymbol{\theta})(x,y) = \mathbf{g}_{l,r}(a_0 + a_1 x + a_2 y, b_0 + b_1 x + b_2 y) \tag{5}$$

Here $\boldsymbol{\theta}=(a_0,a_1,a_2,b_0,b_1,b_2)^T$ contains six geometric model parameters. To solve $\boldsymbol{\theta}$, we employ the least squares criteria, which has the following minimization cost function:

$$E(\boldsymbol{\theta}) = \left\| \mathbf{g}_{k,r} - f_{k,r}(l,\boldsymbol{\theta}) \right\|_2^2 \tag{6}$$

The motion vector $\boldsymbol{\theta}$ can be solved with the Gaussian–Newton optimization method.

Now, consider the motion estimation of a hyperspectral image. The multiple bands in a hyperspectral image provide more information than a single band, which leads to improved accuracy of the motion information [28]. The underlying premise is, for any hyperspectral image sequence, the motion between adjacent frames for each band is exactly the same. In practice, however, when motion estimation is performed on each band independently, the motion information will differ among the bands. A representative motion field must be chosen for all the bands. Tom and Katsaggelos studied the motion estimation methods of a color image sequence, which included a single-band method, vector mean method, vector median method and simultaneous motion estimation method with all three bands, and concluded that the simultaneous method performed best [29]. A computational efficiency problem arises when the simultaneous motion estimation method is directly extended to the hyperspectral image case, because of the high dimensionality of the hyperspectral image. Therefore, we modify the simultaneous motion estimation method with the primary components of the hyperspectral image, greatly reducing the number of spectral bands in the motion estimation process. Thus, we can get the following minimization cost function:

$$E(\boldsymbol{\theta}) = \sum_{r=1}^{R_1} \left(w_r \times \left\| \mathbf{g}'_{k,r} - f'_{k,r}(l,\boldsymbol{\theta}) \right\|_2^2 \right) \tag{7}$$

where $\mathbf{g}'_{k,r}$ and $f'_{k,r}(l,\boldsymbol{\theta})$ represent the rth principal component of $\mathbf{g}_k$ (the kth hyperspectral observation) and $f_k(l,\boldsymbol{\theta})$ (the prediction of $\mathbf{g}_k$ from frame l with motion vector $\boldsymbol{\theta}$). w_r represents the weight of the rth component and is set as $w_r=\alpha^{r-1}$, $0<\alpha<1$, $r=1,\ldots,R_1$, to give a component decaying effect to the overall cost function. A Gaussian–Newton optimization method is also used to resolve the motion vector $\boldsymbol{\theta}$.

4. Image reconstruction algorithm

4.1. PCA-based HSI resolution enhancement

In this paper, all the principal components of the hyperspectral image are divided into three groups: primary components, secondary components and noise components. According to the amount of information and noise they contain, different image resolution enhancement techniques are selected for the different groups:

(a) Primary components contain most of the information of the hyperspectral image, which makes the resolution enhancement of the primary components quite

important for that of the original hyperspectral image. Furthermore, the number of spectral bands of the primary components is usually relatively small; therefore, super-resolution reconstruction is utilized for resolution enhancement of the primary components.

(b) Secondary components contain a small portion of the information of the hyperspectral image and a certain amount of noise. As the number of spectral bands of the secondary components is relatively large, it is time-consuming to conduct super-resolution reconstruction for the secondary components. Because of the limited amount of information, the resolution enhancement of the secondary components does not have so much effect as the primary components. Therefore, it is reasonable to employ efficient cubic interpolation for the secondary components, to make their size the same as the super-resolved primary components.

(c) The amount of information contained in the noise components is very small and the amount of noise is quite large. It is natural to conduct a denoising procedure on the noise components to reduce the amount of noise contained in the original hyperpsectral image. A 7×7 neighborhood median filter is performed on the noise components because of its efficiency and effectiveness. After that, cubic interpolation is also used to make the size of the noise components the same as the super-resolved primary components.

4.2. MAP-based SRR problem formulation

This section briefly introduces the super-resolution reconstruction method of the primary components. Let the primary components of the kth low-resolution hyperspectral observation be denoted by $\ddot{\mathbf{g}}'_k=\{\mathbf{g}'_{k,1},\mathbf{g}'_{k,2},\ldots,\mathbf{g}'_{k,R_1}\}$, the full set of the P primary components by $\ddot{\mathbf{g}}'=\{\ddot{\mathbf{g}}'_1,\ddot{\mathbf{g}}'_2,\ldots,\ddot{\mathbf{g}}'_P\}$ and the primary components of the desired high-resolution hyperspectral image by $\ddot{\mathbf{z}}'=\{\mathbf{z}'_1,\mathbf{z}'_2,\ldots,\mathbf{z}'_{R_1}\}$. The purpose of this is to realize the MAP estimate of the HR primary components $\ddot{\mathbf{z}}'$, given the sequence of low-resolution primary components $\ddot{\mathbf{g}}'$. The estimate can be computed by

$$\hat{\ddot{\mathbf{z}}}'=\arg\max\{p(\ddot{\mathbf{z}}'|\ddot{\mathbf{g}}')\} \tag{8}$$

Applying Bayes' rule, (8) becomes

$$\hat{\ddot{\mathbf{z}}}'=\arg\max\left\{\frac{p(\ddot{\mathbf{g}}'|\ddot{\mathbf{z}}')p(\ddot{\mathbf{z}}')}{p(\ddot{\mathbf{g}}')}\right\} \tag{9}$$

Since $p(\ddot{\mathbf{g}}')$ can be considered a constant and can be eliminated from the optimization problem in (9), it can be rewritten as

$$\hat{\ddot{\mathbf{z}}}'=\arg\max\{p(\ddot{\mathbf{g}}'|\ddot{\mathbf{z}}')p(\ddot{\mathbf{z}}')\} \tag{10}$$

Using the monotonic logarithm function, it can be expressed as

$$\hat{\ddot{\mathbf{z}}}'=\arg\max\{\log p(\ddot{\mathbf{g}}'|\ddot{\mathbf{z}}')+\log p(\ddot{\mathbf{z}}')\} \tag{11}$$

Assuming the low-resolution observations are independent, we obtain

$$\hat{\ddot{\mathbf{z}}}'=\arg\max\left\{\sum_k^P \log p(\ddot{\mathbf{g}}'_k|\ddot{\mathbf{z}}')+\log p(\ddot{\mathbf{z}}')\right\} \tag{12}$$

Noting that the components of $\ddot{\mathbf{g}}'_k$ and $\ddot{\mathbf{z}}'$ are statistically independent, respectively, (12) can be written as

$$\hat{\ddot{\mathbf{z}}}'=\arg\max\left\{\sum_r^{R_1}\left(\sum_k^P \log p(\mathbf{g}'_{k,r}|\mathbf{z}'_r)+\log p(\mathbf{z}'_r)\right)\right\} \tag{13}$$

Usually, the model noise in (3) is assumed to be AWGN with variance σ^2, thus the likelihood distribution $p(\mathbf{g}'_{k,r}|\mathbf{z}'_r)$

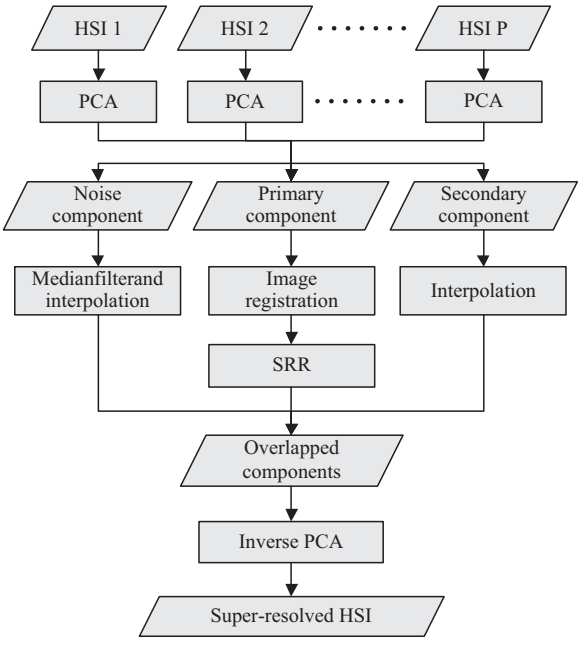

Fig. 1. Diagram of the whole SRR procedure flow.

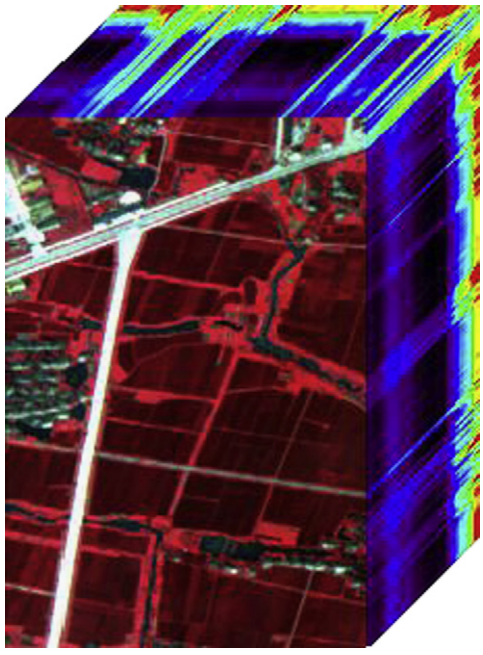

Fig. 2. Xiaqiao PHI hyperspectral image cube.

can be given by

$$p(\mathbf{g}'_{k,r}|\mathbf{z}'_r)=\frac{1}{C_1}\exp\left(-\frac{\|\mathbf{g}'_{k,r}-\mathbf{DBM}_k\mathbf{z}'_r\|_2^2}{2\sigma^2}\right) \tag{14}$$

where C_1 is a constant.

The prior distribution function $p(\mathbf{z}'_r)$ imposes the spatial constraints on the component. A total variation (TV) prior model [30,31] is employed here to regularize this problem, and can be expressed as

$$p(\mathbf{z}'_r)=\frac{1}{C_2}\exp\left(-\frac{1}{\beta}\Gamma(\mathbf{z}'_r)\right) \tag{15}$$

Table 1
Motion estimation errors.

Methods	NMSE	Time (s)
Vector mean	0.000434	85
Vector median	0.006860	84
The proposed method	0.000046	31

where C_2 is also a constant, and β is the temperature parameter. $\Gamma(\mathbf{z}'_r)$ stands for the standard TV norm, which looks like:

$$\Gamma(\mathbf{z}'_r)=\int_\Omega\sqrt{|\nabla\mathbf{z}'_r|^2+\theta}\,dx\,dy \tag{16}$$

where Ω is the two-dimensional image space, and θ is a small positive parameter which ensures differentiability when $\nabla\mathbf{z}'=0$. Thus, the discrete expression is written as

$$\Gamma(\mathbf{z}'_r)=\sum_i\sum_j\sqrt{|\mathbf{z}'_r(i,j)_x|^2+|\mathbf{z}'_r(i,j)_y|^2+\theta} \tag{17}$$

where $\mathbf{z}'_r(i,j)_x=\mathbf{z}'_r(i+1,j)-\mathbf{z}'_r(i,j)$ and $\mathbf{z}'_r(i,j)_y=\mathbf{z}'_r(i,j+1)-\mathbf{z}'_r(i,j)$.

Substituting (14) and (15) into (13), after some manipulation, the super-resolution reconstruction of the primary components is equivalent to the minimization of the following regularization problem:

$$\hat{\mathbf{z}}'=\arg\min\left\{\sum_r^{R_1}\left(\sum_k^P\|\mathbf{g}'_{k,r}-\mathbf{DBM}_k\mathbf{z}'_r\|_2^2+\lambda\Gamma(\mathbf{z}'_r)\right)\right\} \tag{18}$$

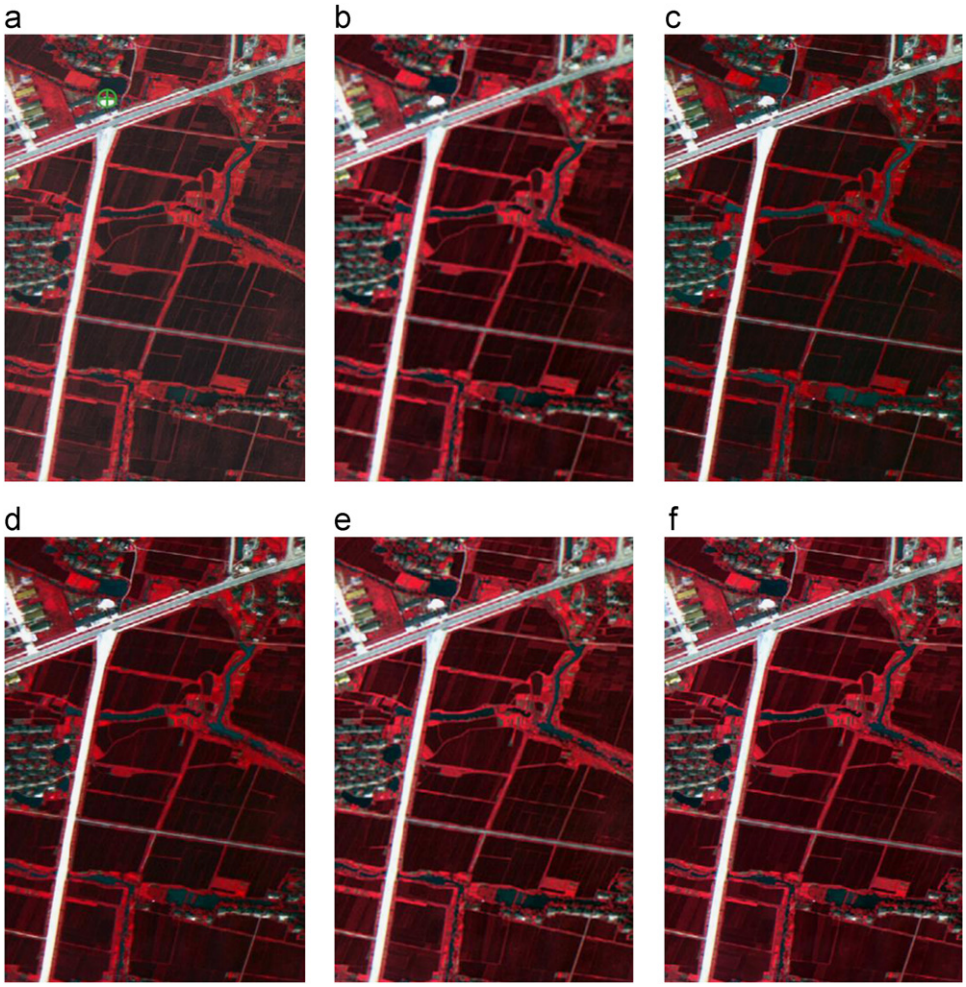

Fig. 3. Experimental results of the Xiaqiao remote sensing hyperspectral image (R: 48, G: 31, B: 11): (a) original hyperspectral image, (b) cubic interpolation, (c) Gram–Schmidt fusion, (d) PC fusion, (e) maximum entropy SRR method and (f) the proposed SRR method.

The parameter λ is the regularization parameter, which controls the contribution of the prior term relative to the data fidelity term. As the Euler–Lagrange equations of the cost function shown in (18) is nonlinear with respect to $\hat{\mathbf{z}}'$, the lagged diffusivity fixed-point iteration introduced in [32] is utilized. Then, a gradient descent

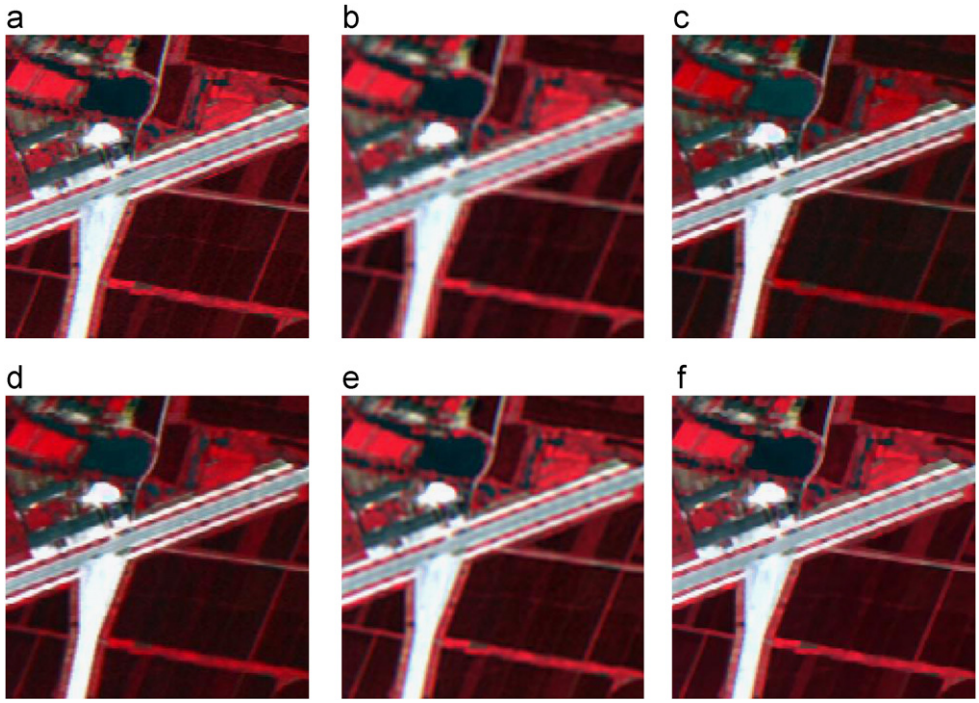

Fig. 4. (a–f) Detailed regions cropped from Fig. 3(a)–(f), respectively: (a) original hyperspectral image, (b) cubic interpolation, (c) Gram–Schmidt fusion, (d) PC fusion, (e) maximum entropy SRR method and (f) the proposed SRR method.

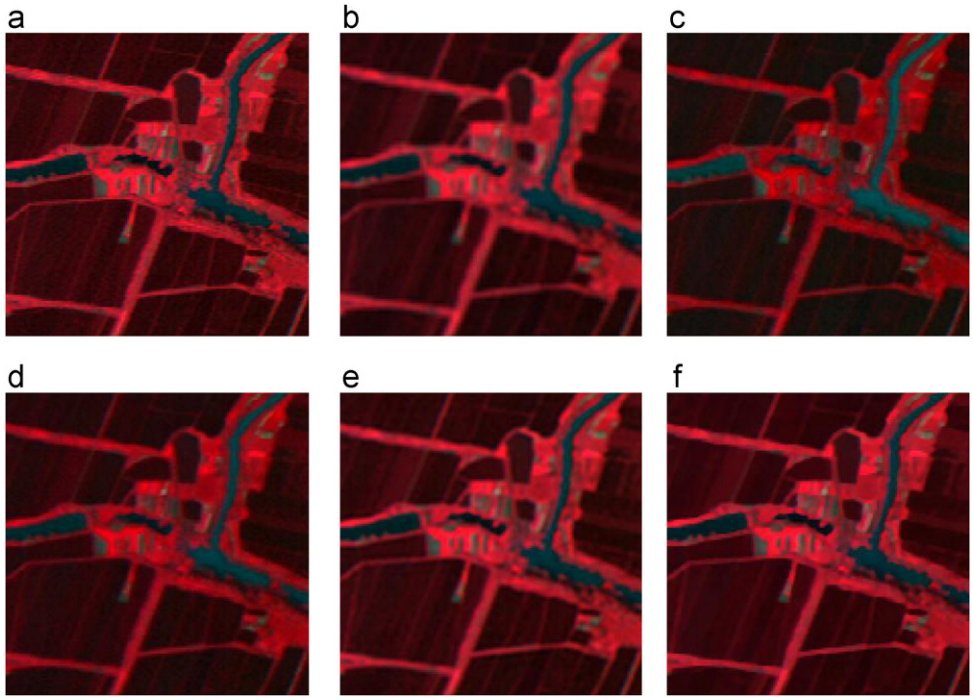

Fig. 5. (a–f) Detailed regions cropped from Fig. 3(a)–(f), respectively: (a) original hyperspectral image, (b) cubic interpolation, (c) Gram–Schmidt fusion, (d) PC fusion, (e) maximum entropy SRR method and (f) the proposed SRR method.

method is used to solve the cost function. The matrices **D**, **B**, $\mathbf{M}_k$ and their corresponding transposes are interpreted as direct image operators in the computation process [20,33]. Thus, it is not necessary to generate large matrices, and the proposed algorithm can be implemented efficiently.

4.3. Procedure flow

The overall procedure flow of the SRR for hyperspectral images can be implemented by the following steps:

Step (*1*): Apply PCA transforms to each hyperspectral image, respectively, and obtain their corresponding principal components.

Step (*2*): Determine parameters R_1 and R_2 and divide the principal components into three groups: primary components, secondary components and noise components.
Step (*3*): Perform simultaneous motion estimation with the primary components to obtain the motion field between the hyperspectral image sequences.
Step (*4*): Apply super-resolution reconstruction to the primary components and obtain the corresponding super-resolved primary components.
Step (*5*): Employ cubic interpolation to the secondary components with the same size as the super-resolved primary components.
Step (*6*): Conduct a 7×7 neighborhood median filter on the noise components to remove noise in the hyperspectral image, and then interpolate to the same size as the super-resolved primary components.

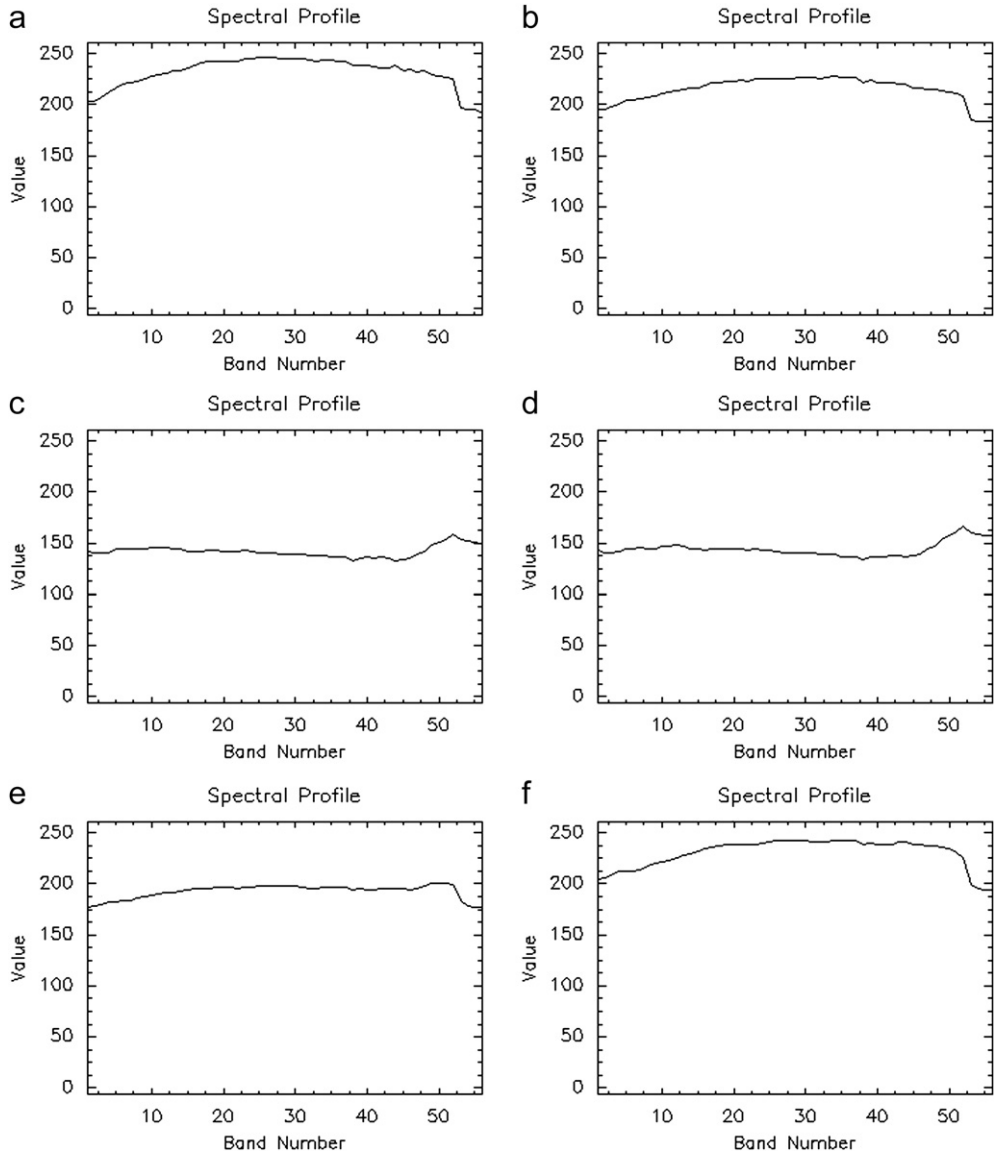

Fig. 6. Spectral curvatures of the typically shown point in Fig. 3(a): (a) original hyperspectral image, (b) cubic interpolation, (c) Gram–Schmidt fusion, (d) PC fusion, (e) maximum entropy SRR method and (f) the proposed SRR method.

Step (7): Apply the inverse PCA transform to the overlap of the super-resolved primary components, interpolated secondary components and noise component, obtaining the super-resolved hyperspectral images.

A block diagram of the whole procedure flow is shown in Fig. 1.

5. Experimental results

5.1. Experimental setup

Four different sets of experiments were conducted with the proposed algorithm. The first one is a simulated experiment for a hyperspectral remote sensing image with known motion parameters, and the last three are real experiments for hyperspectral image sequences with unknown motion parameters, which are estimated with the proposed motion estimation method. For the simulated experiment, the following three quantitative measures were employed to evaluate the proposed SRR algorithm for hyperspectral images:

$$MSE(r)=\frac{\|z_r-\hat{z}_r\|_2^2}{L_1N_1\times L_2N_2} \tag{17}$$

$$PSNR(r)=10\times\log\left(\frac{255^2\times L_1N_1\times L_2N_2}{\|z_r-\hat{z}_r\|_2^2}\right) \tag{18}$$

$$SAM(i)=\arccos\left(\frac{\langle u_{z(i)},u_{\hat{z}(i)}\rangle}{\|u_{z(i)}\|_2\times\|u_{\hat{z}(i)}\|_2}\right) \tag{19}$$

where z_r and $\hat{z}_r$ are the rth band of the original and reconstructed high-resolution hyperspectral images, respectively, and $L_1N_1\times L_2N_2$ denotes the dimension of one band of the high-resolution hyperspectral image. $MSE(r)$ and $PSNR(r)$ denote the mean squared error (MSE) and peak signal noise ratio (PSNR) for band r, respectively, so the global MSE and $PSNR$ are computed by averaging over all the bands. Let $u_{z(i)}$ and $u_{\hat{z}(i)}$ denote the spectral vector of the ith pixel of the original and reconstructed high-resolution hyperspectral images, respectively, so $SAM(i)$ represents the spectral angle mapper (SAM) of the ith pixel, and the global SAM is computed by averaging over the whole image. The regularization parameter selection method in this paper is that several different regularization parameters are employed and the parameter value corresponding to the best result is chosen.

5.2. Simulation results

The hyperspectral image used in this experiment is a remote sensing image collected with an airborne imaging spectrometer (PHI) from the Xiaqiao test site. A total of 56 bands of the PHI image (of size 346×512) were utilized, and the spectral ranges were from 440 nm to 854 nm. Fig. 2 shows the original PHI hyperspectral image cube. The LR hyperspectral image sequence was obtained by the following steps: (1) the original hyperspectral image was shifted, in both the horizontal and vertical directions, to produce four shifted hyperspectral images; (2) the sequence was convolved with a Gaussian smooth filter PSF of size 3×3 with variance equal to 0.5; (3) it was then downsampled in both the horizontal and vertical directions by the factor of two; (4) lastly, zero-mean Gaussian-noise was added to the sequence. In order to compare our method with other panchromatic/hyperspectral image fusion methods, one high-resolution panchromatic image was created by spectrally integrating over the entire spectral range with the original hyperspectral image [1].

Firstly, the performance of the presented simultaneous motion estimation method in Section 3 is validated. We implement the simultaneous motion estimation method using the primary components of the synthetic hyperspectral

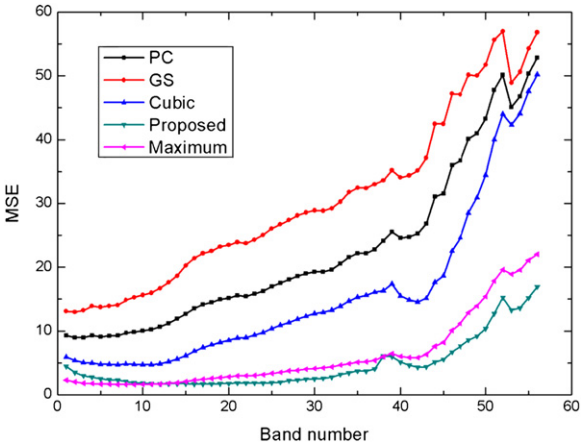

Fig. 7. MSE evaluation of each band of the experimental results versus the band number.

Table 2
Quantitative evaluation results of the experimental images.

	Cubic interpolation	Gram–Schmidt fusion	PC fusion	Maximum entropy method	The proposed SRR method
MSE	15.42	30.13	22.27	6.12	4.62
PSNR	36.25	33.34	34.65	40.26	41.48
SAM	1.83	2.29	2.12	1.42	1.38

Table 3
Land-cover classes and associated numbers of pixels used in this classification procedure.

Class name	Number of labeled samples
Road	77
Corn	81
Vegetable	42
Grass	46
Water	66
Soil	76
Total number of labeled samples	388

images. The corresponding parameters are set as: $R_1=3$ and $R_2=10$. In this part, the vector mean and vector median, after the separate motion estimation of each band, were selected as the benchmark of the presented method. Table 1 shows the errors and time span of the three methods. It is clear that the proposed method achieves the lowest NMSE error and uses the shortest time span, the reasons for which are twofold. First, the primary components contain most of the

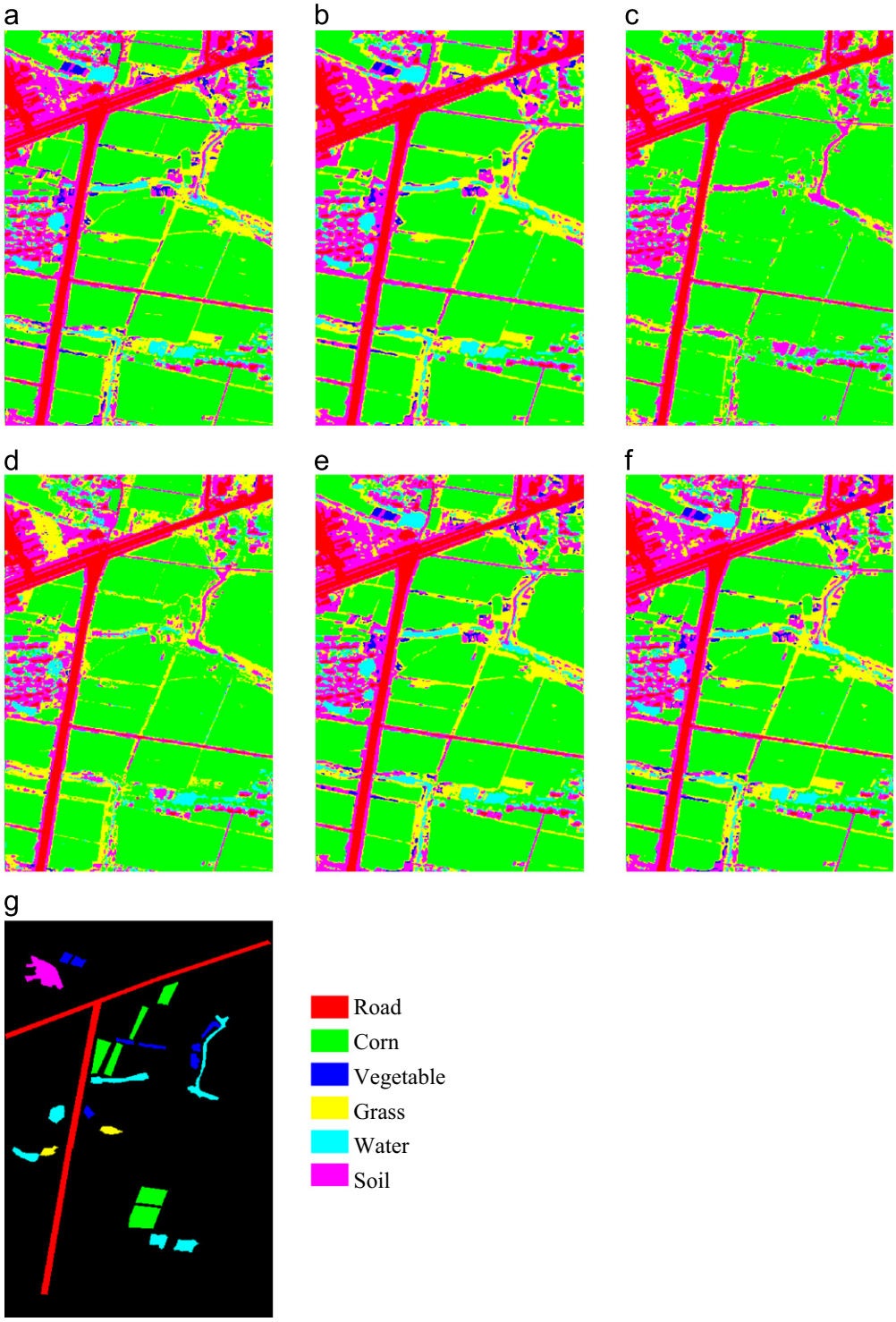

Fig. 8. SVM supervised classification results of the Xiaqiao remote sensing hyperspectral image: (a) original hyperspectral image, (b) cubic interpolation, (c) Gram–Schmidt fusion and (d) PC fusion.

information of the hyperspectral image and provide more information than a single band, which supports improved accuracy of the motion field. Second, the number of bands of the primary components is just three, which is much smaller than the number of spectral bands of the original hyperspectral image, and, therefore, greatly reduces the computational load of the motion estimation process.

The next issue is the evaluation and analysis of the reconstructed images, which are shown in Figs. 3 and 4 with a color composite of 48(R), 31(G) and 11(B). The experimental results of the cubic interpolation, Gram–Schmidt fusion, PC fusion and maximum entropy-based hyperspectral image super-resolution reconstruction method in [22] are used as benchmarks for the proposed algorithm. The original hyperspectral image and cubic interpolation results are shown in Fig. 3(a) and (b), respectively. Fig. 3(c) and (d) are the Gram–Schmidt fusion and principal component (PC) fusion results, respectively. Fig. 3(e) and (f) illustrate the results of the maximum entropy SRR method and the proposed SRR algorithm. The resolution enhancement factor is two, in both the horizontal and vertical directions. The regularization parameter is set as $\lambda=0.4$. We analyze the experimental results from both the spatial and spectral aspects. To facilitate the spatial comparison, detailed regions cropped from Fig. 3(a)–(f) are shown in Fig. 4(a)–(f), respectively. Evidently, the spatial resolution of both the fusion results and the SRR results are significantly improved, in comparison with the interpolation results.

The spectral information preservation is the other issue at hand. Another set of detailed regions, cropped from Fig. 3(a)–(f), are shown in Fig. 5(a)–(f), respectively. It is clear that the color of the fusion results changes a lot compared with the original hyperspectral image, that is to say, the spectral information is destroyed in the image fusion process. To facilitate the comparison of the spectral information, we select one typical point, as shown in Fig. 3(a), and draw the spectral curvatures of the experimental results in Fig. 6. From the figures, it is clearly observed that the spectral curvatures of the fusion methods change a lot, when compared with the original hyperspectral image. The spectral curvatures of the cubic interpolation method and the maximum entropy SRR method change a little, while the spectral curvature of the proposed SRR method is almost the same as that of

Table 4
Quantitative evaluation results of the classification images.

	Original image	Cubic interpolation	Gram–Schmidt fusion	PC fusion	Maximum entropy method	The proposed SRR method
OA	90.23%	89.39%	64.36%	73.33%	90.07%	90.17%
Kappa	0.8700	0.8590	0.5227	0.6451	0.8678	0.8692

Fig. 9. Experimental results of the letter paper sequence (R:1, G:23, B:46): (a) LR image, (b) bilinear interpolation, (c) cubic interpolation, (d) maximum entropy SRR method and (e) the proposed SRR method.

Fig. 10. (a–d) Detailed regions cropped from Fig. 9(b)–(e), respectively (R: 1, G: 23, B: 46): (a) bilinear interpolation, (b) cubic interpolation, (c) maximum entropy SRR method and (d) the proposed SRR method.

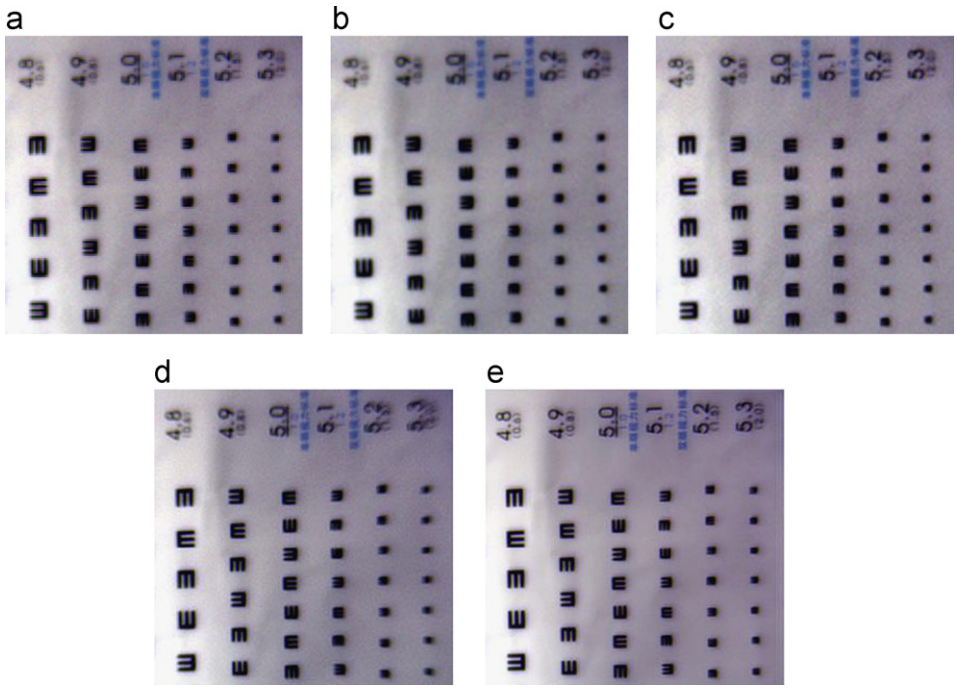

Fig. 11. Experimental results of the visual chart sequence (R: 40, G: 31, B: 11): (a) LR image, (b) bilinear interpolation, (c) cubic interpolation, (d) maximum entropy SRR method and (e) the proposed SRR method.

the original hyperspectral image. To further compare the spectral preservation properties of the different methods, Fig. 7 is given to show the MSE evaluation of each band of the experimental results versus the band number. It is observed that the SRR methods have much lower MSE values on all the bands, and the proposed method has better results than the maximum entropy SRR method on most bands, which further validates the excellent spectral preservation property of the proposed method.

Table 2 lists the quantitative evaluation results of the experimental images using MSE, PSNR and SAM, respectively. Generally speaking, it is clearly observed that the SRR methods achieve better quantitative evaluation results than the fusion methods and the interpolation method, in terms of all the objective quantitative measures. The proposed SRR method definitely achieves a slightly better evaluation result than the maximum entropy SRR method. Although the image fusion methods obtain a higher spatial resolution than the cubic interpolation method, their quantitative evaluation results are worse than those of the cubic interpolation method. The main reason for this is that the spectral information is destroyed in the fusion process. From all the above comparisons of the experimental results, it can be clearly seen that the proposed method not only enhances the spatial resolution of the hyperspectral image effectively, but also preserves spectral properties very well. It is concluded that the proposed SSR method provides a better result than the other resolution enhancement methods, in terms of both spatial and spectral aspects.

In order to further validate the effectiveness of the proposed hyperspectral image SRR method, a classification procedure was conducted on the resolution-enhanced hyperspectral images. Six representative classes, namely, road, corn, vegetable, grass, water, and soil, were considered. Table 3 gives the number of labeled samples for each class obtained from the original hyperspectral image. All 56 bands were used for classification.

Fig. 8 shows the support vector machine (SVM) supervised classification result of the Xiaqiao PHI image. To evaluate the classification accuracy, a test field map is shown in Fig. 8(g), based on the ground reference data. The classification accuracies for the six image results are given in Table 4. From the table, it is observed that the image fusion result has a poor classification result, the reason for which is that the spectral properties are destroyed in the image fusion process. Because of the excellent spectral preservation ability, the proposed hyperspectral image

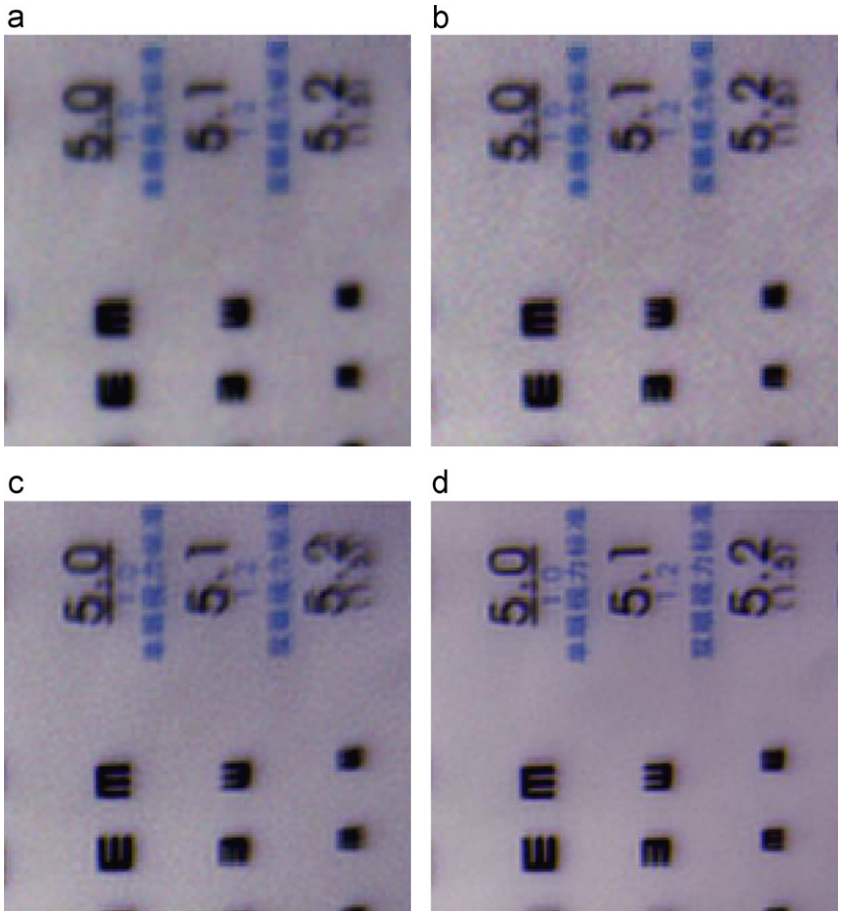

Fig. 12. (a–d) Detailed regions cropped from Fig. 11(b)–(e), respectively (R: 40, G: 31, B: 11): (a) bilinear interpolation, (b) cubic interpolation, (c) maximum entropy SRR method and (d) the proposed SRR method.

SRR method has the highest classification accuracy, which approximates to the classification result of the original hyperspectral image.

5.3. Real results

To further illustrate the performance of the proposed method, it was tested on three real data sets. The real hyperspectral image sequences used in these three experiments were collected using the Nuance-NIR imaging spectrometer. The acquired hyperspectral images have 46 bands, with spectral ranges from 650 nm to 1100 nm, with a 10 nm spectral interval. As there is no real high-resolution panchromatic image, image fusion experiments cannot be implemented here. We conduct the maximum entropy SRR method with the motion parameters between the real hyperspectral images estimated using the proposed motion estimation method. We compare the results of the proposed SRR method with those of the maximum entropy SRR method and the interpolation methods via visual evaluation.

5.3.1. Letter paper sequence

In the first real image experiment, we select the letter paper hyperspectral image sequence. Seven hyperspectral images (of size 220×100) are used in the experiment to obtain a resolution enhancement factor of two. The fourth frame, shown in Fig. 9(a) with a color composite of 1(R), 23(G) and 46(B), is selected as the reference frame. The camera blur kernel is assumed to be a 3×3 Gaussian kernel with variance equal to 0.5 for all the bands. The corresponding parameters for SRR are set as: $R_1=3$, $R_2=10$ and $\lambda=0.42$. Fig. 9(b)–(e) shows the results of bilinear interpolation, the cubic interpolation, the maximum entropy SRR method and the proposed SRR method, respectively. To facilitate a spatial comparison, detailed regions cropped from Fig. 9(b)–(e) are shown in Fig. 10(a)–(d), respectively. By visual comparison, it is observed that the results of the proposed SRR method are clearer than those of the single-frame interpolation methods and the maximum entropy SRR method. Furthermore, as the noise components are filled with zeros in the reconstruction process, the proposed SRR result is less noisy.

5.3.2. Visual chart sequence

Our second real experiment uses the visual chart sequence. Five LR hyperspectral observations of size 140×140 are used with a resolution enhancement factor of two. The third frame is selected as the reference frame, which is shown in Fig. 11(a) with a color composite of 40(R), 31(G) and 11(B). The blur kernel is assumed to be a 3×3 Gaussian kernel with variance equal to 0.5. The corresponding parameters are set as $R_1=3$, $R_2=10$ and $\lambda=0.45$. The results of bilinear interpolation, cubic interpolation, the maximum entropy SRR method and the proposed SRR method are given in Fig. 11(b)–(e), respectively. Detailed regions cropped from Fig. 11(b)–(e) are shown in Fig. 12 (a)–(d), respectively. It is clearly seen that the proposed SRR result is more desirable than those of the other methods.

5.3.3. Building sequence

Our third real hyperspectral image resolution enhancement experiment uses four building images, with the first frame as the reference frame shown in Fig. 13(a). The resolution enhancement factor is set as two. The corresponding parameters are set as $R_1=3$, $R_2=10$ and $\lambda=0.45$. Fig. 13(b)–(e) shows the results of bilinear interpolation, cubic interpolation, the maximum entropy SRR

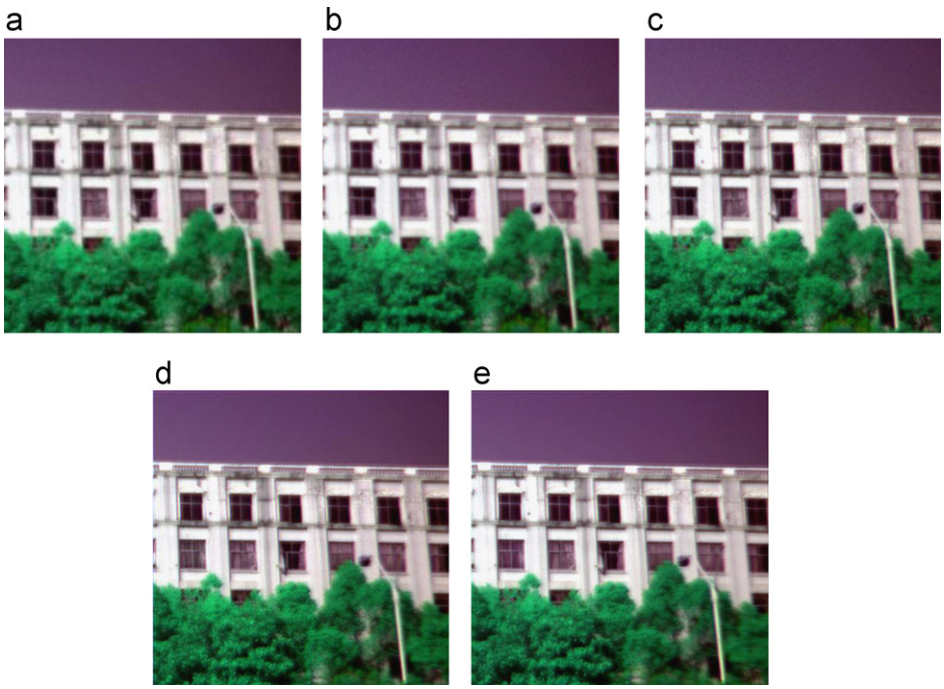

Fig. 13. Experimental results of the building sequence (R:1, G:11, B:31): (a) LR image, (b) bilinear interpolation, (c) cubic interpolation, (d) maximum entropy method and (e) the proposed SRR method.

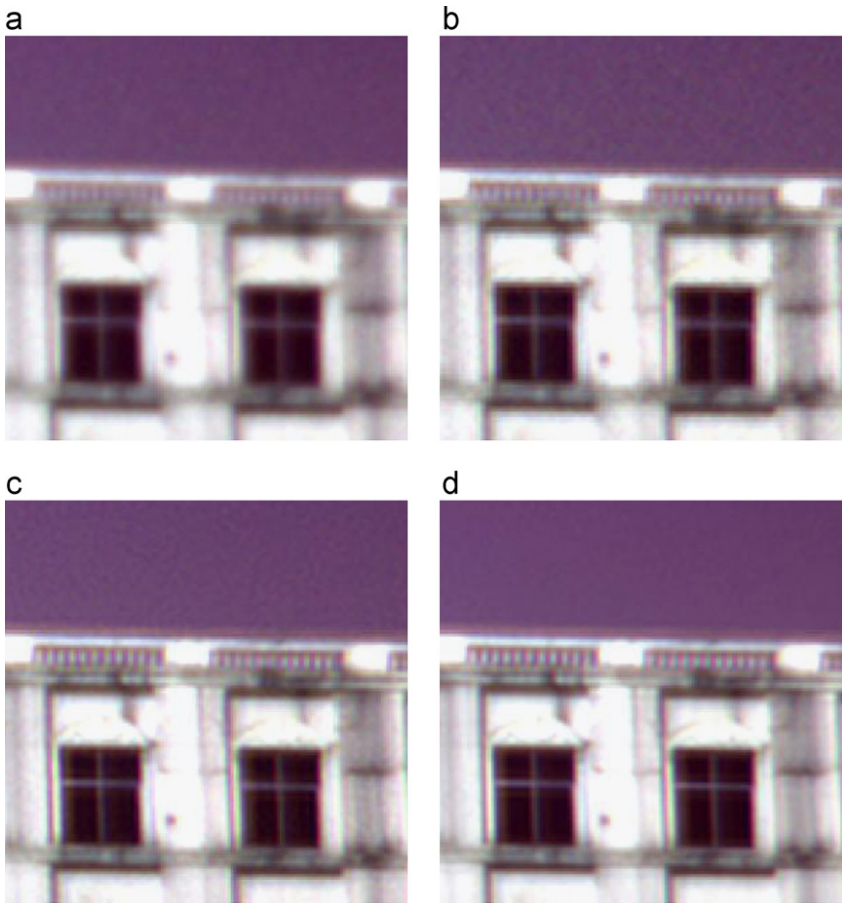

Fig. 14. (a–d) Detailed regions cropped from Fig. 13(b)–(e), respectively (R: 1, G: 11, B: 31): (a) bilinear interpolation, (b) cubic interpolation, (c) maximum entropy SRR method and (d) the proposed SRR method.

method and the proposed SRR method, respectively. Detailed regions cropped from Fig. 13(b)–(e) are shown in Fig. 14(a)–(d), respectively. It is clear that the proposed method achieves better results than the other hyperspectral image resolution enhancement methods.

6. Conclusions

This paper has proposed a multi-frame super-resolution algorithm for real hyperspectral images, in which PCA is utilized in both the motion estimation and image reconstruction processes. In the motion estimation counterpart, primary components, which contain most of the information of a hyperspectral image, are used, supporting high accuracy of the motion estimation process. In the image reconstruction counterpart, different image resolution enhancement techniques are applied to different groups of components, according to the amount of information contained in the principal components, in order to simultaneously reduce computational load and remove hyperspectral image noise. The proposed algorithm was tested on different sets of synthetic images and real hyperspectral image sequences. Experimental results confirmed that the proposed algorithm outperforms interpolation methods and image fusion methods, in terms of both the quantitative measurements and visual evaluation.

However, the proposed algorithm still has room for improvement. For example, the algorithm could be extended to spaceborne remote sensing hyperspectral images, which is more complicated and difficult because of the complicated remote sensing imaging conditions. These problems are the main focus of our future work.

Acknowledgments

This work was supported in part by the National Basic Research Program of China (973 Program) under Grant no. 2011CB707105, by the National Natural Science Foundation of China under Grants 40930532, 41071269 and 40971220, by Post-doctoral Science Foundation of China under Grant 2011M501242. The authors would like to thank Professor Bjørn K. Alsberg from Norwegian University of Science and Technology for this sharing of the maximum entropy SRR program. The authors would also like to thank the anonymous reviewers who gave very helpful comments.

References

[1] M. Eismann, R. Hardie, Application of the stochastic mixing model to hyperspectral resolution enhancement, IEEE Transactions on Geoscience and Remote Sensing 42 (9) (2004) 1924–1933.

[2] S.C. Park, M.K. Park, M.G. Kang, Super-resolution image reconstruction: a technical overview, IEEE Signal Processing Magazine 20 (3) (2003) 21–36.

[3] S. Farsiu, D. Robinson, M. Elad, P. Milanfar, Advances and challenges in super-resolution, International Journal of Imaging System and Technology 14 (2) (2004) 47–57.

[4] R.Y. Tsai, T.S. Huang, Multi-frame image restoration and registration, Advanced in Computer Vision and Image Processing 1 (1984) 317–339.

[5] S.P. Kim, N.K. Bose, H.M. Valenzuela, Recursive reconstruction of high resolution image from noisy undersampled multiframes, IEEE Transactions on Acoustics, Speech, and Signal Processing 38 (2) (1990) 1013–1027.

[6] S. Rhee, M.G. Kang, Discrete cosine transform based regularized high-resolution image reconstruction algorithm, Optical Engineering 38 (8) (1999) 1348–1356.

[7] R.H. Chan, T.F. Chan, L. Shen, Z. Shen, Wavelet algorithms for high-resolution image reconstruction, SIAM Journal of Scientific Computing 24 (4) (2003) 1408–1432.

[8] M.K. Ng, C.K. Sze, S.P. Yung, Wavelet algorithms for deblurring models, International Journal of Imaging Systems and Technology 14 (3) (2004) 113–121.

[9] H. Ur, D. Gross, Improved resolution from sub-pixel shifted pictures, CVGIP: Graphical Models and Image Processing 54 (1992) 181–186.

[10] M. Irani, S. Peleg, Improving resolution by image registration, CVGIP: Graphical Models and Image Processing 53 (1991) 231–239.

[11] H. Stark, P. Oskoui, High-resolution image recovery from image plane arrays, using convex projections, Journal of the Optical Society of America A: Optics and Image Science, and Vision 6 (1989) 1715–1726.

[12] A.J. Patti, M.I. Sezan, A.M. Tekalp, Superresolution video reconstruction with arbitrary sampling lattices and nonzero aperture time, IEEE Transactions on Image Processing 6 (8) (1997) 1064–1076.

[13] X. Zhong-qiang, Z. Xiu-chang, Super-resolution reconstruction of compressed video based on adaptive quantization constraint set presented at the First International Conference on Innovative Computing, Information and Control, 2006.

[14] R.R. Schultz, R.L. Stevenson, Extraction of high-resolution frames from video sequences, IEEE Transactions on Image Processing 5 (6) (1996) 996–1011.

[15] L.C. Pickup, D.P. Capel, S.J. Roberts, A. Zisserman, Bayesian image super-resolution, continued, Advances in Neural Information Processing Systems (2006) 1089–1096.

[16] H. Shen, L. Zhang, B. Huang, P. Li, A MAP approach for joint motion estimation, segmentation, and super resolution, IEEE Transactions on Image Processing 16 (2) (2007) 479–490.

[17] M. Elad, A. Feuer, Restoration of a single superresolution image from several blurred, noisy, and undersampled measured images, IEEE Transactions on Image Processing 6 (12) (1997) 1646–1658.

[18] M. Elad, A. Feuer, Superresolution restoration of an image sequence: adaptive filtering approach, IEEE Transactions on Image Processing 8 (3) (1999) 387–395.

[19] X. Huang, L. Zhang, P. Li, Classification and extraction of spatial features in urban areas using high resolution multispectral imagery, IEEE Geoscience Remote Sensing Letters 4 (2) (2007) 260–264 .

[20] L. Zhang, H. Zhang, H. Shen, P. Li, A super-resolution reconstruction algorithm for surveillance images, Signal Processing 90 (3) (2010) 848–859.

[21] T. Akgun, Y. Altunbasak, R.M. Mersereau, Super-resolution reconstruction of hyperspectral images, IEEE Transactions on Image Processing 14 (11) (2005) 1860–1875.

[22] B. Buttingsrud, B. Alsberg, Superresolution of hyperspectral images, Chemometrics and Intelligent Laboratory Systems 84 (2006) 62–68.

[23] F. Mianji, Y. Zhang, H.K. Sulehria, Super-resolution challenges in hyperspectral imagery, Information Technology Journal 7 (7) (2008) 1030–1036.

[24] M. Eismann, R. Hardie, Hyperspectral resolution enhancement using high-resolution multispectral imagery with arbitrary response functions, IEEE Transactions on Geoscience and Remote Sensing 43 (3) (2005) 455–465.

[25] Q. Yuan, L. Zhang, H. Shen, P. Li, Adaptive multiple-frame image super-resolution based on U-curve, IEEE Transactions on Image Processing 19 (12) (2010) 3157–3170.

[26] T. Jolliffe, Principal Component Analysis, Springer-Verlag, New York, 2002.

[27] G. Chen, S. Qian, Denoising of hyperspectral imagery using principal component analysis and wavelet shrinkage, IEEE Transactions on Geoscience and Remote Sensing 49 (3) (2011) 973–980.

[28] N.R. Shah, A. Zakhor, Resolution enhancement of color video sequences, IEEE Transactions on Image Processing 8 (6) (1999) 879–885.

[29] B.C. Tom, A.K. Katsaggelos, Resolution enhancement of monochrome and color video using motion compensation, IEEE Transactions on Image Processing 10 (2) (2001) 278–287.

[30] L. Rudin, S. Osher, E. Fatemi, Nonlinear total variation based noise removal algorithms, Physica D 60 (1–4) (1992) 259–268.

[31] J. Bioucas-Dias, M. Figueiredo, J. Oliveira, Adaptive Bayesian/total-variation image deconvolution: a majorization-minimization approach, in: European Signal Processing Conference, Florence, Italy, 2006.

[32] C.R. Vogel. Computational Methods for Inverse Problems, SIAM Frontiers in Applied Mathematics, Philadelphia, PA, USA, 2002.

[33] A. Zomet, S. Peleg, Efficient super-resolution and applications to mosaics, Presented at the International Conference on Pattern Recognition, 2000, pp. 579–583.